26/04/2024 05:30

(Article begins on next page)

C: Surfaces, Interfaces, Porous Materials, and Catalysis

Reduction and Oxidation of Maghemite (001) Surfaces: The Role of Iron Vacancies

Giulia Righi, and Rita Magri

Just Accepted

Reduction and Oxidation of Maghemite (001) Surfaces: the Role of Iron Vacancies

Giulia Righi[1,2] *, Rita Magri[1,2]

[1] Department of Physics, Informatics, and Mathematics of the University of Modena and Reggio-Emilia

[2] CNR-S3 Institute of Nanoscience, via Campi 213/A, 41125 Modena, Italy

Abstract

The knowledge of surface reduction and oxidation energetics in reducible oxides is essential for the design of improved catalysts for oxidation reactions. This is particularly true for iron oxides, a very attractive material system because of the availability and biocompatibility of its constituents. In this work by means of density functional theory (DFT) we have thoroughly studied the γ-Fe_2O_3 (001) maghemite surfaces, taken fully account of the iron vacancies beyond a mean field approach. Despite the structurally similarity with the more studied magnetite Fe_3O_4 surfaces, from which maghemite differs only for the presence of iron vacancies in the octahedral sites, and for the absence of reduced Fe^{2+} cations, the surface properties are quite different. Our investigation shows that the presence of Fe vacancies is responsible for an increase in the surface reducibility. Also, it favors surface oxidation. The main reason is that the Fe vacancies cause a decrease of the electronic charge of the surface oxygen atoms, which become then more reactive. We have considered different surface terminations and found that the reduced surfaces are more stable than the simple bulk-truncated ones. The reduction leads to a new reconstruction of the surface which is the most stable surface termination among those investigated. We have examined the charge transfers and the modifications in the electronic structure caused by the surface reduction.

I. Introduction

Iron and Oxygen are two of the most plentiful elements on Earth, and, consequently, many studies have been aimed to investigate the potential of iron oxides for a large number of applications. Iron oxides have been indeed proposed for sustainable energy storage [1] [2], biotechnology [3], data sensors, biomedicine [4]. In the field of clean energy production an important role is played by electrochemical devices for the utilization of alternative, environmentally friendly fuels, and iron-oxides have the potential to make a substantial contribution as electrodes in such devices. The possibility to use iron oxides as new catalytic electrode materials in substitution to the existing costly and rare raw materials (i. e. platinum), without loosing in efficiency and maintaining an high level of performance is highly attractive.

Many catalytic reactions, as for example CO oxidation, follow the Mars-Van Krevelen mechanism [5]. In this mechanism the surface is reduced with a surface oxygen atom transferred to an adsorbed fuel molecule. This reaction is then followed by the surface re-oxidation with the refilling of the oxygen vacancy from an O_2 molecule from the gas-phase. The mechanism thus requires an easy transfer of oxygen atoms from and to the catalyst surface. Reducible oxides, such as iron oxides, can thus be effective catalysts for these reactions.

In this paper we study the reduction and oxidation properties of the maghemite (γ-Fe_2O_3) iron oxide as determined by the extraction and addition of oxygen atoms from and to the surface. Maghemite surfaces have been shown to have a high potential for applications. Recently, Qiu et al. [6] have shown experimentally that maghemite exhibits promises for oxygen reduction reactions (ORR), a fundamental reaction taking place in living systems and at the cathodes of electrochemical devices [7]. Najafishirtari et al. [8] have observed that larger the percentage of the maghemite phase over the hematite one, α-Fe_2O_3, in dumbbell shaped metal/iron-oxide nanocrystalline catalysts, more reactive were the catalysts towards CO conversion. Furthermore, iron-oxides in the maghemite phase have recently been proposed as cathode or anode materials for lithium iron batteries, which need to be improved for their extensive use in hybrid electric vehicles and new devices [9] [1].

Maghemite (γ-Fe_2O_3) is the second most stable iron oxide [10]. It is obtained by the oxidation [11] or as a weathering product [12] of magnetite (Fe_3O_4), which is the most stable (in conditions of ultra-vacuum) and studied iron oxide. Maghemite and magnetite are structurally correlated [13]. They have both an inverse spinel crystal structure with two kinds of differently coordinated Fe atoms: iron atoms coordinated to oxygen atoms in octahedral sites, and iron atoms with a tetrahedral coordination to oxygen atoms. Contrary to magnetite, where all the tetrahedral iron atoms have oxidation state Fe^{3+} and an equal number of Fe^{3+} and Fe^{2+} cations occupy the octahedral sites, in γ-Fe_2O_3 all the iron atoms are in a trivalent oxidation state. To guarantee the neutrality of the bulk structure some Fe vacancies are required, that have experimentally been found to be located at the octahedral sites [14].

Several experimental works [15] [16] [17] [18] suggested that the iron vacancies of maghemite are arranged in an ordered structure corresponding to the tetragonal space group $P4_12_2$ with a=8.347 Å and c=25.042 Å. Recently, Crespo et al. [12], using a DFT approach and a supercell containing three magnetite bulk unit cells, compared the total energies of all the structures obtained by occupying differently the 24 Fe octahedral sites with 8/3 vacancies. They found that the structure with space group $P4_12_2$ is indeed the most stable. The supercell corresponded to thrice the cubic unit cell of the magnetite bulk, replicated along the [001] direction, so as to accommodate an integer number of iron vacancies.

Along the [001] direction of this crystalline structure, the maghemite and magnetite bulks correspond to the alternation of octahedral Fe and oxygen planes and of tetrahedral Fe planes. In the ordered structure with $P4_12_2$ space group the Fe vacancies are located in two (octahedral Fe – oxygen) planes out of three as shown in Fig. 1.
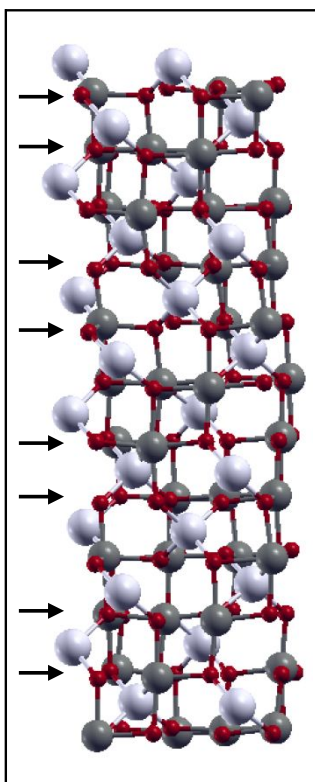
Fig. 1 Maghemite ($\gamma - Fe_2O_3$) bulk. Dark and light grey balls are the octahedral and tetrahedral iron atoms, respectively. Red balls are the oxygen atoms. Arrows indicate the planes where the iron vacancies are located.

To study the thermodynamics of oxygen release and adsorption on the maghemite (001) oriented surfaces we have considered two surfaces terminated with octahedral iron atoms and oxygen atoms, obtained by truncating the bulk. These surfaces terminations have been shown in magnetite to be more stable than the surfaces terminated in tetrahedral iron atoms [19], thus, because of the structural similarity between the two phases, we assume that this is also true for maghemite. Of the two considered surfaces, one, termed A, has the iron vacancies on the outermost plane, while the other, termed B, has the iron vacancies located in the third plane below the outermost plane. We have also considered an additional surface reconstruction related to a new stable reconstruction of the (001) magnetite surface, found recently in a joint experimental and theoretical work [20].

We have investigated the reduction and oxidation properties of these surfaces in order to understand the role of the iron vacancies, and analyzed the corresponding changes in the electronic properties and related charge transfers. We have compared the results obtained for the maghemite surfaces with those of analogous calculations performed for the corresponding (001) surfaces of magnetite where the iron vacancies are

absent. These are the first calculations for maghemite surfaces which take account explicitly of the iron vacancies beyond a mean-field approximation treatment[21] [22].

II. Method

II.1 Computational Details

Calculations based on the density functional theory (DFT) have been carried out using the Quantum Espresso Package [23] [24]. We have used ultrasoft pseudopotentials to describe the interaction between the iron and oxygen ions and the valence electrons, and the approach of Perdew, Burke, and Ernzerhof (PBE) [25] for the exchange-correlation functional. We used a 4 x 4 x 1 Monkhorst - Pack (MP) grid of k-points to integrate the electronic charge [28]. The energy cutoffs for the wavefunction and charge density expansions were set to 40 Ry and 420 Ry, respectively. The calculations were spin polarized.

To describe the electronic properties of the localized electron states in iron oxides we have used the Hubbard correction (DFT+U) using the implementation of Cococcioni et al. [26]. The U value for the iron atoms was set to 4 eV, a value which allows us to reproduce the experimental bulk properties.

We have calculated the maghemite bulk lattice parameters obtaining a = 8.42 Å, and c = 25.19 Å . The calculated magnetic moment per unit cell is 2.5 μ_B. These values are in agreement with those calculated by Crespo et al. [12] and with the experiments [17] [16] [29] . In order to estimate the charge transfers caused by the creation of oxygen vacancies, or by the addition of oxygen atoms to the surfaces, we have calculated the Bader charges [30] on the atoms in the different structural configurations. To investigate the occupation of the orbitals we have used the Löwdin charge [31] [32] .

The surfaces have been modeled through periodically arranged symmetric slabs separated by 21 Å of vacuum, sufficient to make negligible the couplings between the periodic replicas. The x,y dimensions of the unit cell were kept fixed to the optimized bulk parameter. The atomic positions in the slabs were optimized using the Broyden-Fletcher-Goldfarb-Shanno algorithm (BFGS) as implemented in the PW.x code until the forces were less than 0.01 eV/ Å. The atoms of the central plane were kept fixed to their bulk positions. The total energy criterion for the structural optimization was set to 10^{-5} eV.

To model the bulk-truncated surfaces we have extracted portions of bulk (which by itself contains 160 atoms per unit cell). We have considered a sequence of (001) bulk planes stacked, starting from a given central plane, in the same way towards the two surface planes, as shown in Fig. 2. The atom arrangement in the upper and the lower half parts of the slab are the same less an in-plane rotation. In Fig. 2a we show the side views of the slabs corresponding to the two different surface terminations termed A and B. The slabs are formed by 11 and 13 atomic layers, respectively. The planes are labeled O, Ov, and T to indicate octahedral Fe cation and oxygen planes without iron vacancies (O), similar planes but containing iron vacancies on the octahedral sites (Ov), and planes of tetrahedral iron cations (T).

The top views of the surfaces are shown in Fig. 2b. They are both terminated with planes containing octahedral iron cations and oxygen atoms, but, in the A slabs, the iron vacancies (black circles) are in the outermost plane Ov, whereas in the B slabs the iron vacancies (blue circles) are in the third atomic layer below the outermost atomic plane. Both surface terminations are not stoichiometric: indeed the ratio between the number of iron and oxygen atoms is different from the value 2/3 of the maghemite bulk. In the A slab the ratio is 5/8, which is Fe-poorer than the bulk, whereas in the B slab the ratio is 3/4 which is more Fe-richer than the bulk, and it is the same stoichiometry of the magnetite bulk.

The main effect of structural relaxation on the bulk-truncated surfaces is to decrease the octahedral iron and oxygen bond lengths, and to increase the tetrahedral iron and oxygen bond lengths. This leads to a considerable decrease in the total energy.

We have performed calculations for slabs of different thicknesses constructed following the same prescription and supporting the same terminations on the two sides, and found that the convergence of the calculated surface energies with the slab thickness was better than 0.01 eV/Å^2 .

To study the surface reduction we have calculated the oxygen vacancy formation energies as:

$$E_{form} = \frac{1}{2}[E_{slab}(-2O) + E_{O_2} - E_{slab}], \qquad (1)$$

where $E_{slab}(-2O)$ is the energy of the slab with two oxygen vacancies where we have removed one oxygen atom from the top and one from the bottom planes to maintain unchanged the symmetry of the slab, E_{O_2} is the energy of the oxygen molecule, and E_{slab} is the energy of the unreduced surface.

To study the oxidation of the surfaces and determine the most favorable positions for oxygen adsorption, we have calculated the potential energy surfaces (PES) for the oxygen adatom by relaxing the z coordinate of the

adatom together with the surface atoms, and keeping fixed the x and y coordinates of the adatom. The x and y

coordinates belonged to a grid on the surface having a step of 1.05 Å. Once we have individuated the

positions closer to the minima of the energy, we have completed the relaxation releasing further the oxygen

atom in the proximity of those positions, thus finding the precise adsorption site and energy.

In correspondence of the adsorption site we have calculated the adsorption energy as:

$$E_{ads} = \frac{1}{2}[E_{slab}(+2O) - E_{O_2} - E_{slab}], \qquad (2)$$

where $E_{slab}(+2O)$ is the energy of the slab with two oxygen atoms adsorbed, one on the top plane and the

other one on the bottom plane of the slabs at corresponding positions. E_{O_2} is the energy of the oxygen

molecule, and E_{slab} is the energy of the pristine surface.
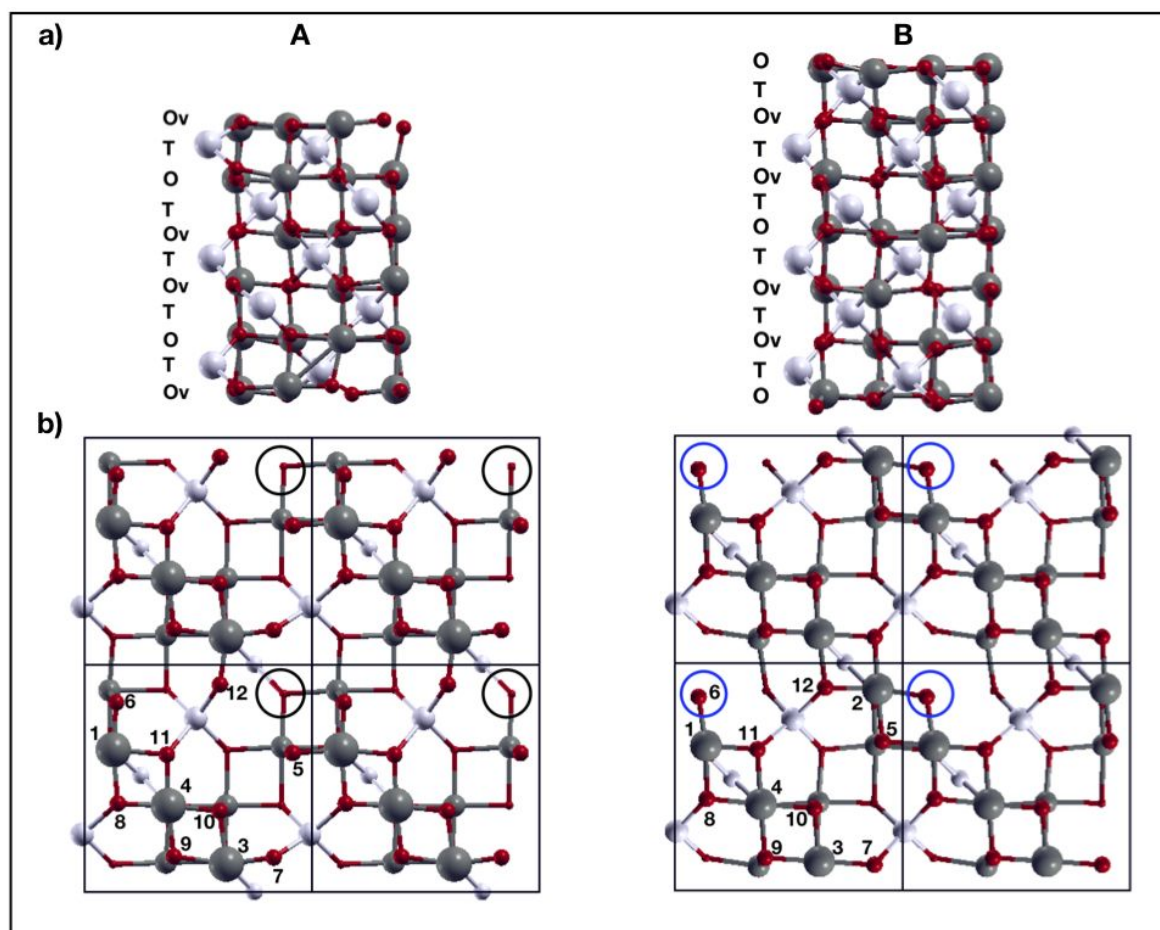
Fig. 2 a) Side view of the slabs used to model the A and B surfaces; b) top view of the (2x2) unit cells of the A and B surfaces. Dark and gray balls are the octahedral and tetrahedral iron atoms, respectively. Red balls are the oxygen atoms. Black and blue circles indicate the sites of the octahedral iron vacancies on the surface (case A), and on the third layer below the outermost plane (case B), respectively. The numbers label the atoms on the outermost layer as explained in the text.

II.2 Calculation of the surface energies

Following the work of Reuter et al. [33] [34], we have calculated the surface energies as functions of the oxygen chemical potential using a thermodynamic formalism combined with the DFT calculations. We summarize here the main equations in relation to maghemite surfaces. The maghemite surface energy $\gamma(T, p)$ at temperature T and pressure p is defined as:

$$\gamma(T,p) = \frac{1}{2A}[G(T,p,N_{Fe},N_O) - N_{Fe}\mu_{Fe}(T,p) - N_O\mu_O(T,p)], \quad (3)$$

where $G(T,p,N_{Fe},N_O)$ is the Gibbs free energy per unit area at temperature T and pressure p, N_{Fe} and N_O are the numbers of iron and oxygen atoms in the system, μ_{Fe} and μ_O are the iron and oxygen chemical potentials appropriate to the physical situation, and A is the surface area. We have neglected the vibrational contribution, negligible at not too high temperatures, so we can approximate $G(T,p,N_{Fe},N_O)$ with the total energy of the slab. We have divided by $2A$ since we have considered symmetric slabs with two equal surfaces.

To derive the chemical potentials of Fe and O we have considered that the surface is in thermodynamic equilibrium with both its bulk and with the gaseous environment. Under this assumption the iron and oxygen chemical potentials are not independent, but they are related by the Gibbs free energy of the maghemite bulk oxide: $G_{Fe_2O_3}^{Bulk} = 2\mu_{Fe}(T,p) + 3\mu_O(T,p)$.

It is conventional to express the surface energies as a function of the oxygen chemical potential, whose values have to satisfy some constraints. Indeed, the possible values of $\mu_O(T,p)$ have to obey the inequality $\frac{1}{3}\Delta H_f(0,0) < \Delta\mu_O < 0$, with $\Delta\mu_O = \mu_O(T,p) - \frac{1}{2}E_{O_2}$. $\Delta H_f(0,0)$ is the heat of formation of the bulk maghemite oxide Fe_3O_2 in the low temperature limit, and E_{O_2} is the energy of the oxygen molecule. The lower boundary is related to the chemical potential of oxygen bonded to Fe in bulk $G_{Fe_2O_3}^{Bulk}$. The chemical potential of oxygen on the surface, being less coordinated than in the bulk, tends to be less negative. The higher boundary reflects a condition of supersaturation of oxygen on the surface which exists only in a gaseous O_2 phase. In correspondence of this value of the oxygen chemical potential, the Fe chemical potential corresponds to that of Fe metal.

As previously seen the lowest limit of $\Delta\mu_O$ is one third of the heat of formation of the maghemite bulk (ΔH_f

(0,0)). Our calculated $\Delta H_f(0,0)$ is -703.67$\frac{KJ}{mol}$. This value is in good agreement with the result

experimentally obtained by Parkinson et al. [35], -711.1 $\frac{KJ}{mol}$.

These considerations apply to the case of zero Kelvin temperature. However, since oxygen is normally in

the gas phase, its properties are more subjected to variations of temperature and pressure. It is therefore

necessary to determine how the oxygen chemical potential depends on temperature T and pressure p.

We assume that the O_2 gas is an ideal gas which acts as a reservoir. We can, consequently, write the

dependence of the oxygen chemical potential on the pressure p at temperature T as $\mu_O(T,p) = \mu_O(T,p^0) + \frac{1}{2}$

$kTln\left(\frac{p}{p^0}\right)$, where p^0 is a reference pressure. For the dependence on temperature at the reference pressure p^0,

we can write $\mu_O(T,p^0)$ as the sum of two terms: $\mu_O(T,p^0) = \frac{1}{2}E_{O_2} + \frac{1}{2}\Delta G_{O_2}(T,p^0)$ [36]. The first term is the value

at $T = 0$ K, whereas the second is half the difference between the Gibbs free energies of the oxygen molecule

at 0 K and at finite temperature T. $\Delta G_{O_2}(T,p^0)$ is linked to the entropy and enthalpy of the O_2 gas. The

values for the entropy and the enthalpy of the oxygen gas are tabulated in Ref. [37] for $p^0 =$ 1 atm. In Fig. S1

we show how the oxygen chemical potential changes as a function of temperature and pressure. Low

temperature and high pressure conditions correspond to high values of the oxygen chemical potential,

whereas high temperature and low pressure conditions correspond to low values of the oxygen chemical

potential.

Thus, each value of $\Delta\mu_0$ in the range indicated above can be made to correspond to a given temperature T

and a given pressure p of the oxygen gas to which the surface is exposed.

III.   Results

III.1 Reduction and Oxidation of the (001) maghemite and magnetite surfaces

The reduction and oxidation properties of maghemite and magnetite surfaces are crucial for estimating their catalytic potential. Consequently, in this section we have investigated the energy required to remove and to add one oxygen atom from/to the surfaces.

We have considered two $Fe_3O_4(001)$ surfaces: the $R45(\sqrt{2} \times \sqrt{2})$ one, which has been considered for many years as the most stable, and it was suggested on the basis of experiments [19] [38] [39] and DFT calculations [40], and the recent reconstruction observed by Bliem et al. [20]. We have considered this last reconstruction because the authors [20] have found that this surface is more stable than the $R45(\sqrt{2} \times \sqrt{2})$ over a wide range of oxygen chemical potential values. Following their notation, we term this surface SCV. In Fig. S2 we show the side (a, b) and top (c, d) views of the two Fe_3O_4 surfaces. Both surfaces are terminated with a plane containing octahedral iron and oxygen atoms. We model the $R45(\sqrt{2} \times \sqrt{2})$ surface with slabs having the same sequence of planes as for the maghemite surfaces, but with all the iron sites occupied, since there are not iron vacancies in magnetite.

In the SVC surface an additional tetrahedral iron atom is inserted in the second layer while two octahedral iron atoms are removed from the third layer below the outermost plane.

Due to the stability of the SCV Fe_3O_4 (001) surface reconstruction, we have considered the same reconstruction also for the (001) maghemite surface that we term SCM_M. As shown in Fig. 3, there are two octahedral iron vacancies (blue circles) in the third layer below the surface, and an additional tetrahedral iron atom above them in the second layer.
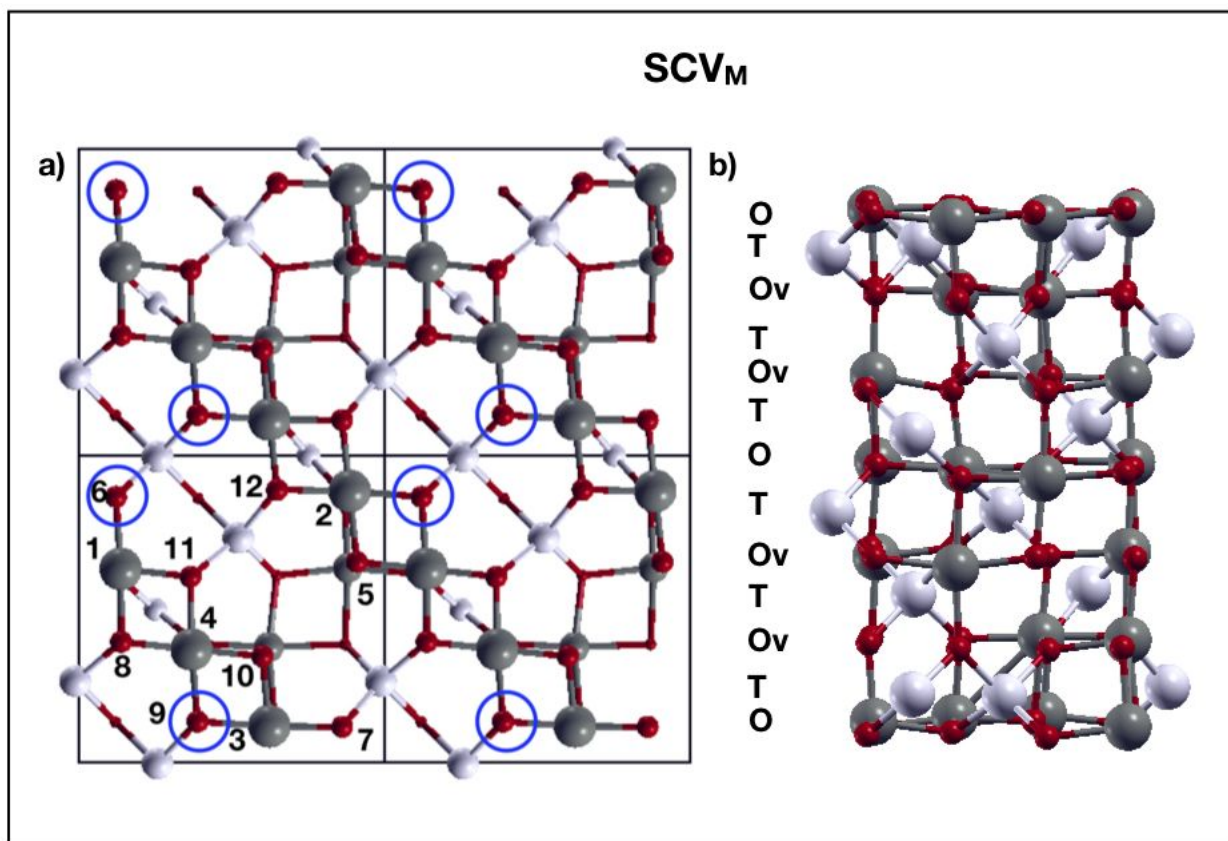
Fig. 3 a) Top view of the (2×2) unit cell of the SCV_M reconstruction of the γ-Fe_2O_3 (001) surface; b) side view of the slab used to model the SVC_M reconstruction of the γ-Fe_2O_3 (001) surface. The color code is the same as in Fig. 2. Blue circles indicate the location of the Fe vacancy in the third layer below the outermost plane. The numbers label the atoms on the outermost layer as explained in the text.

III.1.1 Reduction properties of the maghemite surfaces

First, we report the results on the calculations of the formation energies of the oxygen vacancies on the

bulk-truncated A and B maghemite surfaces. We have classified the surface oxygen atoms according to their

oxygen-iron first-neighbor bonds. The Fe-O bonds were considered first-neighbor if the atom distances were

comprised between 1.7 Å and 2.1 Å. On the surface plane the four Fe atoms are labeled from 1 to 4 (see Fig.

2) and the 8 oxygen atoms are labeled from 5 to 12.

 On both A and B surfaces the oxygen atoms labeled as O_9 and O_{10} are bonded to three octahedral iron atoms (two iron atoms in the same surface layer, and one in the third atomic layer below), while the oxygen atoms labeled O_8 and O_{11} are bonded to two octahedral and one tetrahedral iron atoms.

The other four oxygen atoms have a different first-neighbor coordination on the two A and B surfaces. In the case of the A surface, due to the presence of the iron vacancy on the outermost layer, the atoms O_5 and O_6, are only bonded to two octahedral iron atoms (one on the surface layer and one in the third layer). O_7 and O_{12} also have only two bonds: one to one octahedral iron atom and the other one to one tetrahedral iron atom. On the B surface, instead, atom O_5 is bonded to three octahedral iron atoms, whereas O_6 is the only one with only two bonds to two octahedral irons. Atoms O_7 and O_{12} have the same bonding configuration as atoms O_8 and O_{11}, but their positions with respect to the iron vacancy in the third layer below is different, thus, they are not equivalent to atoms O_8 and O_{11}.

Their vacancy formation energies are reported in Table 1. The oxygen atoms that we have indicated in the Table as equivalent have formation energies for their removal that differ at most of $\pm$ 0.01 eV.

On the magnetite R45($\sqrt{2}$ $\times$ $\sqrt{2}$) surface reconstruction, due to the absence of iron vacancies, there are only two kinds of oxygen atoms: atoms bonded only to octahedral iron atoms, and atoms bonded to both octahedral and tetrahedral iron atoms (see Fig. S2). In the SCV magnetite reconstruction, if we consider again only the first neighbor atomic environment, we have three kinds of oxygen atoms since two oxygen (O_5 and O_{10}) are above the octahedral iron vacancies in the third layer below.

In Table 1 we report the calculated oxygen vacancy formation energies E_{form} also for the magnetite surfaces. The oxygen vacancy formation energies calculated for the oxygen atoms bonded only to the octahedral iron atoms in the R45($\sqrt{2}$ $\times$ $\sqrt{2}$) Fe_3O_4 (001) surface are in agreement with the value, 1.11 eV, calculated by Yu. et al. [41].

Table 1 Formation energy E_{form} of oxygen vacancies on the maghemite A, B, B′, and SCV$_M$ surfaces, and on the R45($\sqrt{2} \times \sqrt{2}$) and SCV magnetite surfaces. The labels of the oxygen atoms are shown in Figs. 2, 3, and Fig. S2. The numbering of the oxygen atoms on the B′ surface is the same as for the B surface apart from the removed oxygen O$_5$. All the formation energies are in eV.

Maghemite A		Maghemite B		Maghemite B′		Maghemite SCV$_M$		Magnetite R45($\sqrt{2} \times \sqrt{2}$)		Magnetite SCV	
O	E_{form}	O	E_{form}	O	E_{form}	O	E_{form}	O	E_{form}	O	E_{form}
5- 6	0.41	5- 6	-0.13	6	2.53	-	-	5-6	1.09	-	-
7-12	1.10	-	-	-	-	6-9	0.38	-	-	5-10	1.77
8-11	2.09	8-12	1.83	8-12	2.22	8-12	1.47	8-12	2.08	8-12	2.32
-	-	7-11	2.50	7-11	2.42	7-11	1.47	7-12	2.08	7-11	2.32
9-10	0.42	9-10	0.85	9-10	1.57	5-10	0.47	9-10	1.09	6-9	1.68

We can observe that, in general, it is easier to remove the oxygen atoms bonded only to octahedral iron atoms, i.e. the atoms indicated as O$_5$-O$_6$-O$_9$-O$_{10}$ in the A, B, and R45($\sqrt{2} \times \sqrt{2}$) surfaces. The energy cost is, indeed, almost 1 eV less than the energy required to extract the oxygen atoms bonded also to tetrahedral iron atoms. Also Yu et al. [41] and Mulakaluri et al. [42] have found that the energy required to create a vacancy on the R45($\sqrt{2} \times \sqrt{2}$) increases if the oxygen is bonded to tetrahedral iron atoms. The only exception is provided by the SVC$_M$ and SVC reconstructions where the two oxygen atoms above the octahedral iron vacancies have a lower E_{form} despite being bonded also to the additional tetrahedral iron. It is, indeed, the proximity of the Fe vacancies that reduces E_{form} .

We have found that the initial electronic charge rearrangement at the surface with respect to the bulk plays a key role in determining the reducibility of the surfaces. In Table 2 we show the variation of the electronic charge of the oxygen atoms at the surfaces compared to the value in the bulks.

Table 2 Variation of the surface oxygen electronic charge in (*e*) with respect to the their bulk value on the studied surfaces.

Maghemite A		Maghemite B		Maghemite B$'$		Maghemite SCV$_M$		Magnetite R45($\sqrt{2} \times \sqrt{2}$)		Magnetite SCV	
O	e	O	e	O	e	O	e	O	e	O	e
5-6	-0.30	6	-0.30	6	< -0.10	-		5-6	< -0.10		-
7-12	-0.25	-	-	-	-	6-9	-0.11	-	-	5-10	< -0.10
8-11	-0.10	8-12	-0.11	8-12	< -0.10	8-12	-0.10	8-12	< -0.10	8-12	< -0.10
-	-	7-11	-0.10	7-11	< -0.10	7-11	<-0.10	7-12	< -0.10	7-11	< -0.10
9-10	-0.30	9-10	-0.11	9-10	< -0.10	5-10	-0.18	9-10	< -0.10	6-9	< -0.10
-	-	5	-0.27	-	-			-	-		-

Comparing Table 1 and 2 we note that it is easier to remove the oxygen atoms whose charge is most diminished with respect to the bulk value. The presence of the iron vacancies on the outermost layer on the A surface causes most of the charge loss for the surface oxygens. On the B and SCV$_M$ surfaces, instead, only the oxygen atoms above the iron vacancies, have less charge. On the other hand, on the R45($\sqrt{2} \times \sqrt{2}$) magnetite surface, just because of the lack of Fe vacancies, the variation of the electronic charge is not significant for all oxygen atoms, and the vacancy formation energy is always larger.

On the SCV Fe_3O_4 (100) reconstruction two octahedral iron vacancies are present in the third layer below, (see Fig. S2), but still there is not a significant variation of the surface oxygen charges with respect to the bulk values. In this case we have found that electronic charge has been transferred to the surface oxygen atoms from the octahedral iron atoms below, which become Fe^{3+} from Fe^{2+}. Fe^{2+} are present only in magnetite and not in maghemite. This explains the lower E_{form} found for SCV$_M$ maghemite reconstruction compared to the SCV magnetite reconstruction for the removal of the corresponding surface oxygen atoms.

Following this rule, it is easier to remove oxygen atoms from the A surface than from the B surface, but there is an important exception. On the B surface the two less charged oxygen atoms will tend to spontaneously leave the surface. The creation of the oxygen vacancies is, indeed, thermodynamically favored since their formation energies are negative. Thus, a more stable reconstruction for the maghemite (001) surface can be obtained from the bulk-truncated B surface by removing one of these oxygen atoms. We term B$'$ this new surface termination.

We also consider the analogously reduced surface structure obtained from the A surface by removing atom O_{10}. This surface is less stable at the temperature T = 0K than the bulk-truncated A surface but it is one of those having the lowest surface energy among the reduced surfaces of the A surface. By analogy with the B$'$ surface we term this reduced surface A$'$.

We have also found a correlation between the value of the vacancy formation energy and the change in the oxidation states of the Fe atoms. The rule is the following: the vacancy formation energy is larger if the electronic charge left behind by the removed oxygen atoms goes to reduce the iron atoms (see Table S1, where the symbol asterisk indicates the Fe atoms that have acquired the oxygen charge). If, instead, the excess charge is acquired by the other less charged oxygen atoms, which become thus closer to the -2 nominative oxygen oxidation state, the creation of the oxygen vacancy is more favored.

On the magnetite surfaces, as shown in Table 2, all the surface oxygen atoms are charged as in the bulk, where they are already in their favorite -2 oxidation state. Thus, the excess of charge, due to the removal of the oxygen atom, always leads to the reduction of Fe atoms. Yu et al. [41] have, indeed, found that, following the creation of the vacancy on the R45($\sqrt{2} \times \sqrt{2}$) surface, two iron atoms increase their electronic charge (+0.39 e), changing their oxidation state. For the same surface, we have calculated an increase of 0.40 e (see Table S1), a value which is in good agreement with theirs.

Since the maghemite B$'$ surface, which has one less oxygen atom, O_5 or, equivalently O_6, see Fig. 2, is more stable than the B surface, we have calculated the formation energy of an oxygen vacancy also for this surface. The results are reported in Table 1. As shown in the table, the creation of the oxygen vacancy on this surface is more unfavored than on the A and B surfaces. In particular, the oxygen O_6, whose vacancy formation energy is small on the A and B surfaces, becomes harder to remove on the B$'$ surface. It is interesting to examine the reconstructed B$'$ surface shown in Fig. 4. O_6, the oxygen partner of the removed

one, because bonded to the same Fe atoms (blue balls in Fig. 4), moves in a bridge position between the two iron atoms, shortening the bond to them. This bond shortening is an indication of bond strengthening. Thus, above the Fe vacancy in the third layer this new structural motif develops on the surface. A similar reconstruction occurs also on the A′ surface, but in this case, the partner of the removed oxygen is located in a neighboring position to the surface Fe vacancy, and its shift to the bridge position is not complete, as shown in Fig. S3.
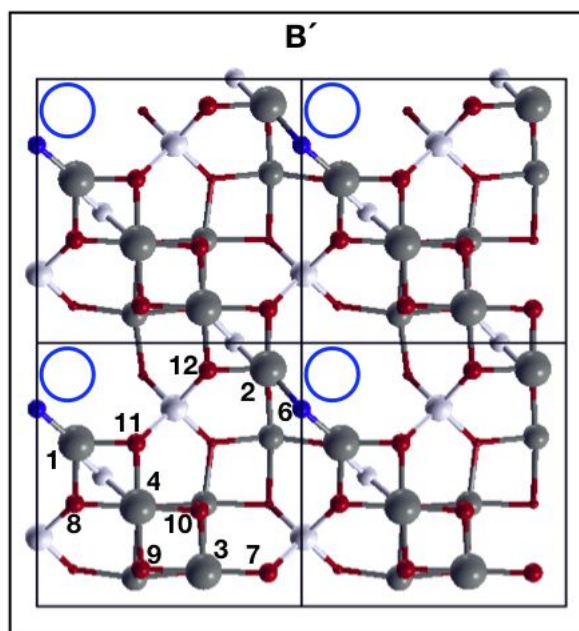

Fig. 4 Top view of the (2×2) unit cell of the B′ surface. Blue circles indicate the Fe vacancy in the third layer below. The blue balls represent the oxygen atoms partner of the removed oxygens. The color code is the same as in Fig. 2. The numbers label the atoms on the outermost layer as explained in the text.

The variation of the charge on the iron atoms following the oxygen removal from the B′ surface is reported in Table S1.

By comparing the vacancy formation energies calculated for the maghemite and magnetite surface reconstructions, we have found that it is easier, in general, to create one oxygen vacancy on the maghemite surfaces than on the corresponding magnetite surfaces (bulk-truncated A-B vs R45($\sqrt{2} \times \sqrt{2}$), SCV$_M$ vs SCV, and most stable B′ vs SCV). Thus, the maghemite (001) surfaces tend to be more reducible than the corresponding magnetite ones. The Fe vacancies and the absence of Fe^{2+} cations play a key role in increasing the reducibility of the maghemite surfaces.

III.1.2 Oxidation properties of the (001) maghemite surfaces

We have calculated the oxidation properties of the maghemite bulk-truncated A and B surfaces, and the reduced B′ surface. In order to determine the preferential adsorption sites for the oxygen atom, we have calculated the Potential Energy Surface (PES) for one oxygen atom adsorbed on the surface. The calculated PES are shown in Fig. 5, where we have reported the positions of the atoms of the first atomic layers. In all the PES the level 0 corresponds to the lowest calculated adsorption energy, and the dark blue areas indicate the most favorite adsorption sites.

For the A surface, one adsorption site sees the added oxygen atom bonded to an octahedral iron atom (Fe_4), in the position indicated by the red cross in Fig. 5a. Following the adsorption, the O_9 atom breaks its bonds with Fe_3 and Fe_4, and creates a new bond with the added oxygen atom forming a dimer as shown in Fig. S4a with an O-O distance of 1.26 Å, slightly larger than the O_2 bond (1.24 Å). The adsorption energy, calculated using Eq. 2, is only 60 meV. Another possible adsorption site is near the iron Fe_3, in the position symmetric to Fe_4 with respect to O_9. In general, as we see from Fig. 5a, other preferential adsorption sites are closer to some of the less charged surface oxygen atoms.

In the case of the B surface, the adatom prefers to bind to the octahedral Fe_4 atom and to a near surface oxygen as indicated by the red cross in Fig. 5b. Following the adsorption, the surface oxygen moves upwards, almost at the same height of the adatom, but, differently than for the A surface, both oxygens remain bonded to their Fe atoms, as shown in Fig. S4b. The O-O distance is now 1.34 Å, larger than the O_2 bond length. The calculated adsorption energy E_{ads} is 0.31 eV, larger than the energy required to adsorb the oxygen on the A surface.

Thus, we see that the adsorption of an oxygen atom on the A and B surfaces leads to the formation of an O-O bond on the surface.

The situation is different on the stable B′ surface, obtained by the B surface by removing O_5. The preferential adsorption site, indicated by the red cross in Fig. 5c, is near the position of the partner oxygen O_6 (blue ball

in Fig. 5c). The added oxygen binds to Fe_1, Fe_2, and to O_6 as shown in Fig. S4 c. The adsorption energy is 0.61 eV, significantly larger than the values calculated on the bulk truncated surfaces. To recover the original B termination, an energy barrier needs to be overcome by the added atom since the oxygen O_6 needs to be pushed to the position of the previous removed oxygen.

It is interesting to look at the charge transfer caused by the adsorption and its relation to the adsorption energy. On the A surface, where most surface oxygens are less charged than on the B surface, one oxygen atom gains a charge +0.2 e becoming closer to the -2 oxidation state. This charge transfer makes the process more favorable. On the contrary on the B and B′ surfaces no oxygen atoms gain electronic charge following the oxygen adsorption.

We have studied the same adsorption process also on the R45($\sqrt{2} \times \sqrt{2}$) Fe_3O_4 surface. In this case the added oxygen binds not to oxygen atoms, but to an octahedral iron atom, as shown in Fig. S4d. The adsorption energy is 0.74 eV, slightly larger than the adsorption energy calculated for the maghemite B′ surface. This behavior is explained by the fact that on the magnetite surface the oxygen atoms are already closer to the -2 oxidation state, and do not need to acquire extra charge.

Thus, our results show that also oxidation is more favored on the maghemite surfaces than on the magnetite one.
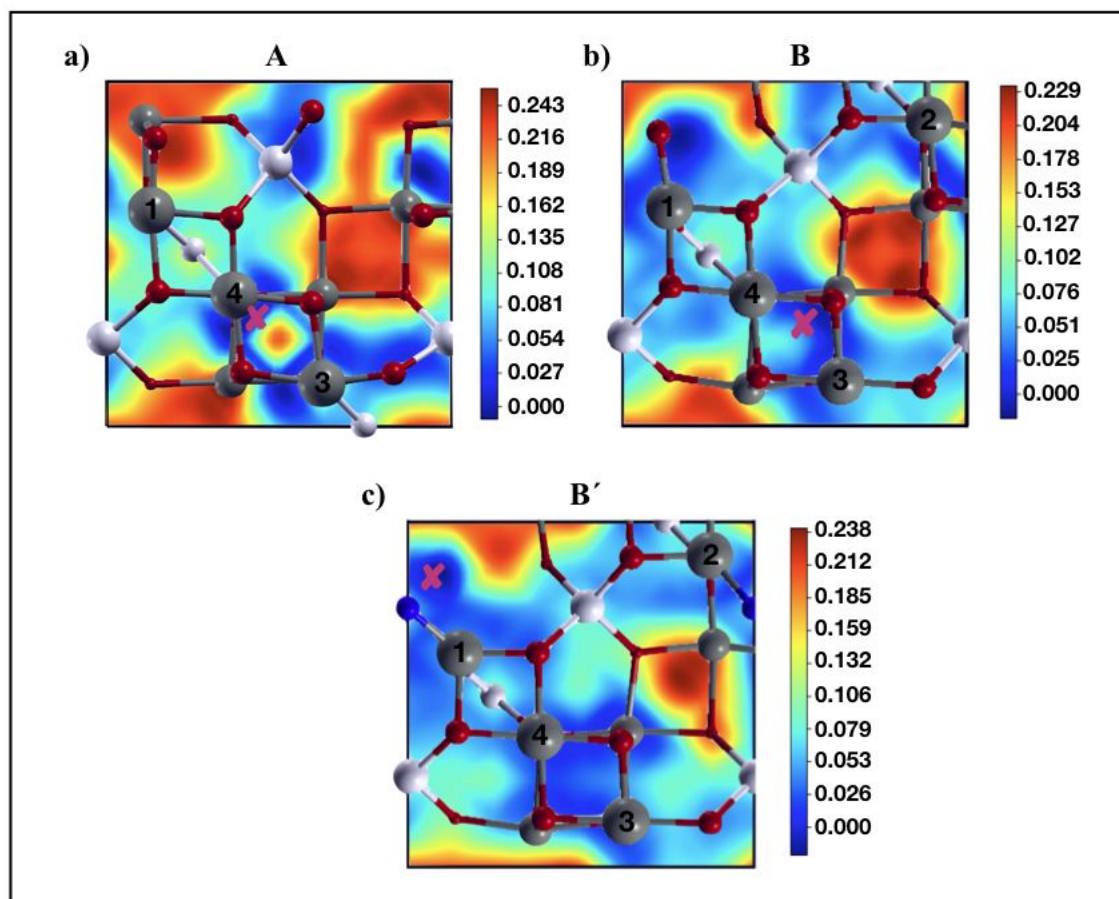
Fig. 5 Potential Energy Surfaces (PES) for one oxygen adatom on the maghemite A, B, and B′ surfaces. The positions of the atoms of the first four layers are shown. Dark and light gray balls are the octahedral and tetrahedral iron atoms, respectively. Red balls are the oxygen atoms. The blue ball is the oxygen atom on B′, that defines the new stable maghemite reconstruction. The crosses on the PES indicate the most favorite adsorption sites. The energy scale is in Ry.

III.2 Surface Energies

We now correlate the reduction properties of the maghemite and magnetite surfaces with their relative stability under ambient conditions.

In Fig. 6a we plot the energies γ of the studied maghemite surfaces: the bulk-truncated A and B surfaces, their reduced A′ and B′ surfaces, B″ which is the reduced B′ surface, the SCV_M and its reduced SCV_M' reconstructions, as a function of the oxygen chemical potential $\Delta\mu_O$. The plot allows us to compare the relative stability of the surfaces, since they have not the same stoichiometry, at the ambient conditions (temperature and pressure of the oxygen gas to which the surface is exposed).
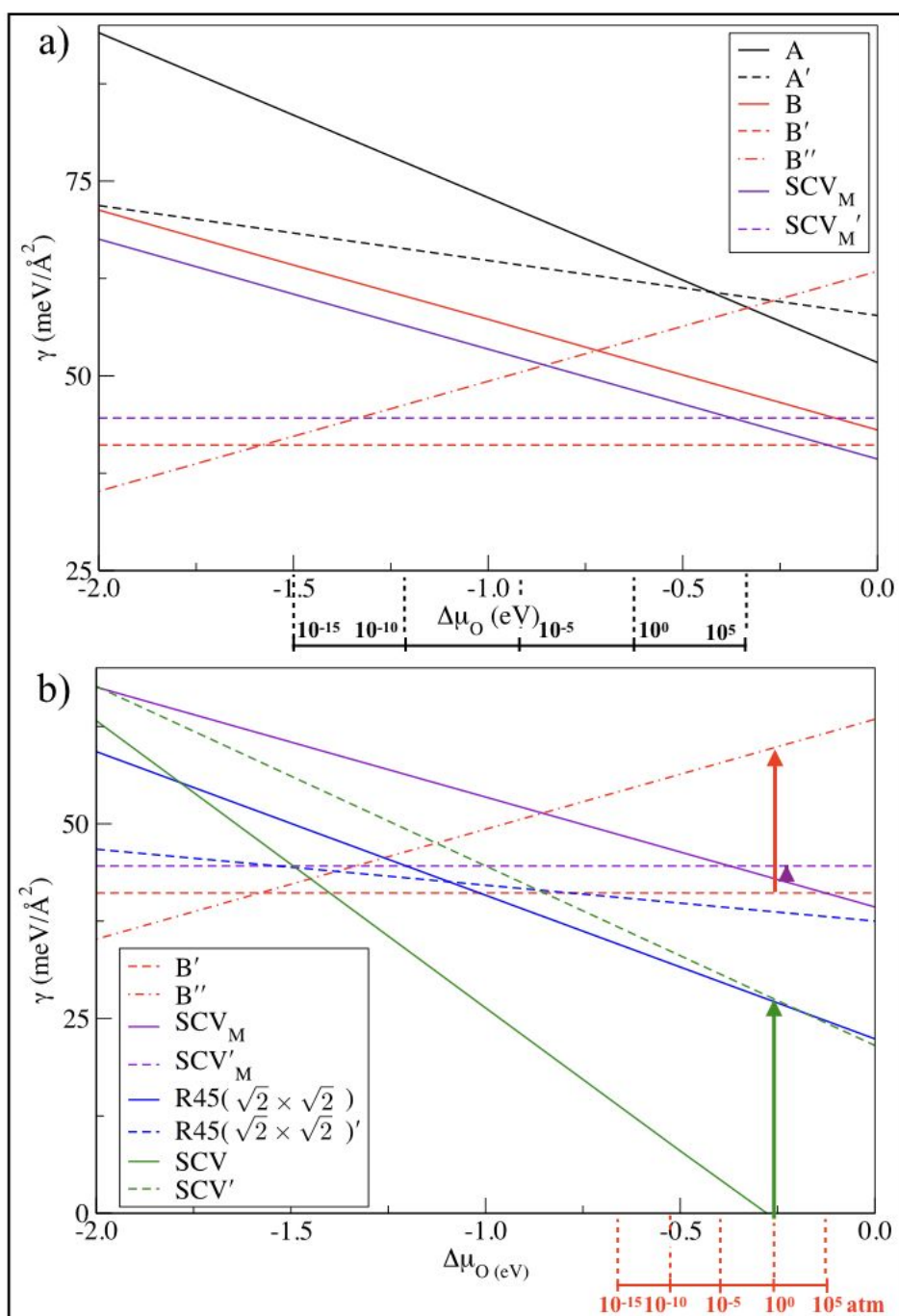
Fig 6 a) Surface Energies γ of maghemite surfaces as a function of the oxygen chemical potential $\Delta\mu_O$. Above the plot we have indicated the values of $\Delta\mu_O$ corresponding to a wide range of pressures (in atm) at the fixed temperature $T = 600$ K. b) Surface Energies γ of the pristine and reduced maghemite and magnetite surfaces as a function of the oxygen chemical potential $\Delta\mu_O$. Below the plot we have indicated the values of $\Delta\mu_O$ corresponding to a wide range of pressures (in atm) at the temperature $T = 300$ K. A and B are the bulk-truncated surfaces, A$'$ and B$'$ their reduced surfaces, and B$''$ is the reduced B$'$ surface. SCV$_M'$ is the reduced SCV$_M$ surface. R45($\sqrt{2} \times \sqrt{2}$) and SCV are two Fe$_3$O$_4$ (001) surfaces, and R45($\sqrt{2} \times \sqrt{2}$)$'$ SCV$'$ are their reduced surfaces. The arrows indicate the energy $\Delta\gamma$ required to pass from a surface to its reduced one.

In the figure we have indicated the interval of the oxygen chemical potential values corresponding to a range of pressure p at a fixed $T = 600$ K. Different experimental groups have indeed synthetized maghemite films [11] [43] at this temperature.

We see that over the range of pressures of interest, the B$'$ surface is the most stable surface. Also the bulk-truncated B surface is more stable than the A one, and this is true also for their reduced surfaces A$'$ and B$'$. Thus, the presence of the iron vacancies on the outermost layer tends to destabilize the surface. The reduced surfaces (A$'$ and B$'$) are more stable than their corresponded bulk-truncated A and B surfaces, so maghemite surfaces will tend to loose surface oxygen atoms.

The oxidized surfaces are more unstable than the pristine surfaces, and, thus, are not reported in the figure.

The SCV$_M$ reconstruction is more stable than the bulk truncated surfaces over all the indicated range of oxygen chemical potentials. At 600 K its reduced SCV$'_M$ surface is even more stable, but not as stable as the B$'$ surface.

From Fig. 6 it can been seen that the B$''$ and SCV$_M$ surfaces can become stable at given values of the oxygen chemical potentials. The reduced B$''$ is the most stable surface only at high temperatures, $T > 600$ K, and low pressures, i.e at $T=1000$ K, p must be lower than 10^{-5} atm. In contrast, the SCV$_M$ surface is stable only at low temperatures, for example at $T=300$ K, p must be at least 10^5 atm, whereas at lower temperatures, lower pressures are permitted.

In Fig. 6b we compare the surface energies of the more stable maghemite B$'$ and SCV$_M$ surfaces with the magnetite R45($\sqrt{2} \times \sqrt{2}$) and SCV ones, together with those of their reduced surfaces. Below we show the range of oxygen chemical potentials corresponding to a range of pressure value p at the temperature $T = 300$ K. At this temperature experimental groups [44] [45] have performed catalytic experiments concerning CO oxidation [44] and hydrogen peroxide decomposition [45]. The length of the vertical arrows at $p = 1$ atm represents the reducibility of the surfaces at this pressure. For the most stable maghemite and magnetite surfaces, B$'$ and SVC, the energy required to reduce the surface is less for the maghemite ($\sim$18.4 meV/Å^2) than for magnetite surface ($\sim$28.3 meV/Å^2). It is interesting to note that at $p = 1$ atm the reduction energy $\Delta\gamma$ is very small for the SCV$_M$ surface ($\sim$1.5 meV/Å^2), which has a surface energy slightly larger than B$'$.

Our results have shown that the reduction and oxidation reactions are in relation with the stability of the surfaces. Indeed, the oxygen vacancy formation energies and the adsorption energies tend to be higher on the most stable maghemite and magnetite surfaces.

III.3 Electronic properties of the surfaces

To understand the trends in surface stability and reduction properties is instructive to look also at the electronic properties of the surfaces. We report in Figs. 7 and S5 the atomic projected density of states (apdos) of the maghemite bulk, of the maghemite bulk-truncated A and B surfaces, and of the most stable B′ surface. The total density of states (dos) and the band structure are shown in Figs. S6 and S7, respectively.

We have also analyzed the variation of the related magnetic moments due to the surface modifications, a phenomenon which is at the heart of the use of iron-oxide nanoparticles as markers in diagnostic biomedicine, since iron-oxides are biocompatible materials [46].

In the apdos we distinguish the electronic states of the spin up and spin down channels, and the contributions due to the surface atoms (indicated with *) and the bulk atoms. We define as bulk atoms the atoms in the center layer of the slabs that we have used to model the surfaces.

As shown in Figs. 7a S6a, and S7a we see that the maghemite bulk is a semiconductor with different energy gaps for the spin up and down channels: 1.80 eV and 1.75 eV, respectively, in reasonable agreement with the experimental value, -2 eV [47]. As for most reducible oxides, the top of the valence band is composed of the oxygen p states, while the bottom of the conduction band is formed by the cation d states. The calculated magnetic moments of the octahedral and tetrahedral iron atoms of the maghemite bulk are 3.73 μ_B and -3.50 μ_B, respectively, and the magnetic moment of the bulk formula unit is 2.5 μ_B, in agreement with the experimental measurements [29]. These values are related to the electronic states of the Fe atoms as shown in the apdos of Fig. 7a. The spin up states of the octahedral and tetrahedral iron atoms are in the valence and conduction band, respectively; and the opposite is true for the spin down states.
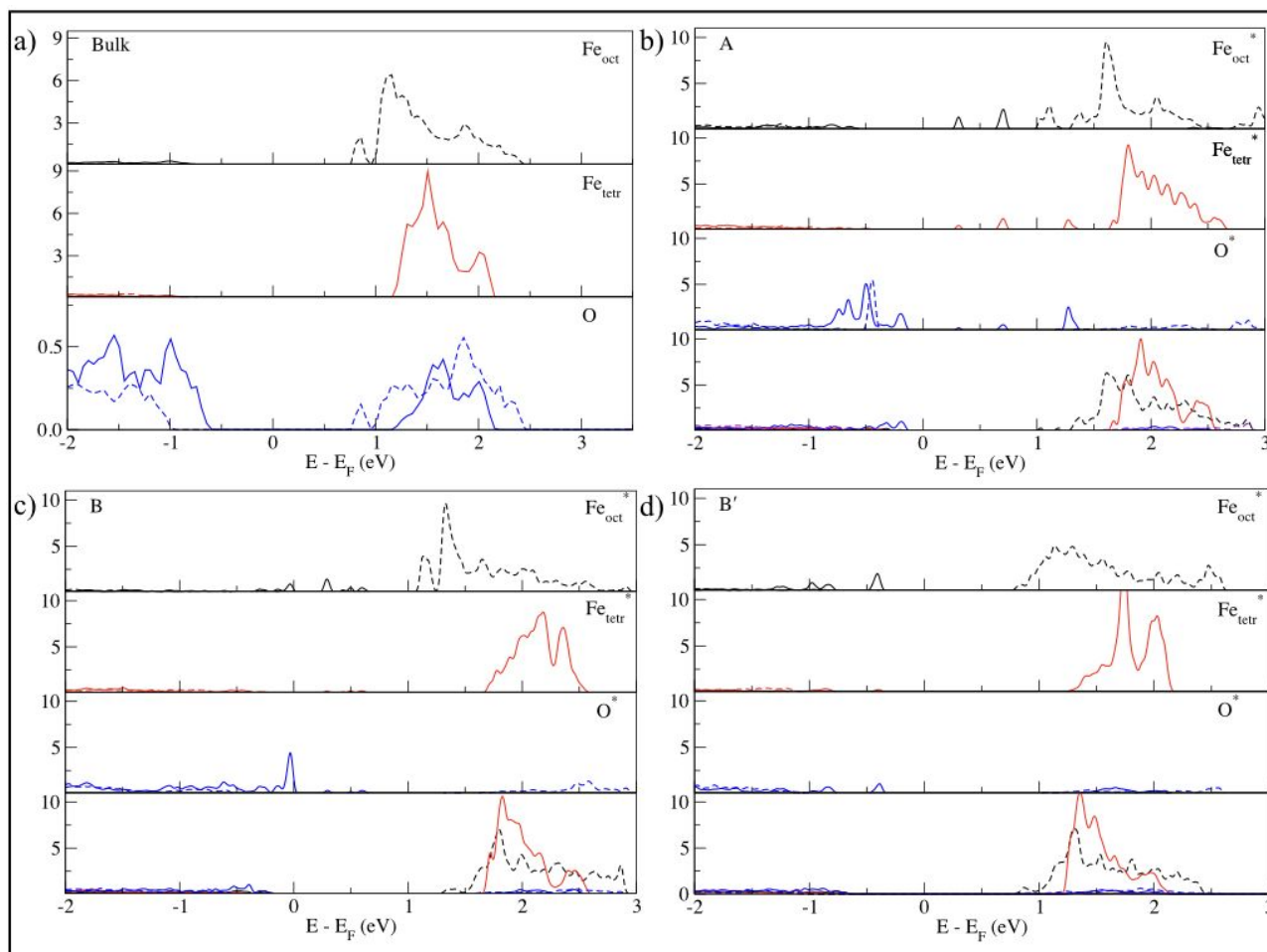
Fig. 7 Atomic projected density of states (apdos) of: a) maghemite bulk, b) A surface, c) B surface, d) and B′ surface. Fe_{oct}^*, Fe_{tetr}^*, and O^* are the surface atoms. Fe_{oct}, Fe_{tetr}, and O are the bulk atoms. Continued and dashed lines are the spin up and down contributions, respectively. The last panel of b), c), and d) shows the apdos of the bulk atoms (middle layer of the slab), and the color code is the same used in a). In panel a) different scales have been used to increase the visibility.

In the apdos of the bulk-truncated A and B surfaces we notice the appearance of new peaks at the bottom of the conduction band related to localized states. To these states contribute only surface atoms, so they are surface states. The A surface is semiconducting with different energy gaps for the spin up and down components: 0.35 and 1.33 eV, respectively, as shown in Figs. 7b, S6b, and S7b. These energy gaps are both smaller than those calculated for the bulk due to the presence of the surface states. Contrary to the A surface, the B surface is not semiconducting. Thus, moving the Fe vacancy from the outermost layer to the third layer below the outermost one causes the surface electronic structure to change significantly. As shown in Figs.

7c,S6c, and S7c , the spin up surface states of the Fe atoms and of the surface oxygen atoms touch the Fermi

Energy. For the spin down contribution we have calculated an energy gap of 1.48 eV, also smaller than in the

maghemite bulk.

The magnetic moments of the surface Fe atoms change with respect to the bulk. In particular, on the A

surface, the magnetic moments of the Fe atoms decrease significantly as shown in Table 3. This is due to the

decrease in the occupation of the spin up states of the octahedral iron atoms in the valence band, and to the

simultaneous increase of the occupation of the spin down states which in the bulk were in the conduction

band. Also two oxygen atoms increase slightly their magnetic moments ($\sim$0.25 μ_B): this increase is related

to the loss of the electronic charge of these oxygen atoms with respect to the bulk. This loss concerns the

charge of only one spin channel.

Table 3 Magnetic Moments (μ_B) and variation of the spin up ($\uparrow$) and down ($\downarrow$) contributions of the Löwdin

charge with respect to the bulk value for the maghemite surfaces.

	Maghemite A			Maghemite B			Maghemite B$'$		
	μ_B	$\uparrow$	$\downarrow$	μ_B	$\uparrow$	$\downarrow$	μ_B	$\uparrow$	$\downarrow$
Fe$_1$	2.93	-0.28	+0.39	3.29	-0.20	+0.20	3.54	-0.03	+0.03
Fe$_2$	/	/	/	3.31	-0.18	+0.19	3.55	-0.02	+0.04
Fe$_3$	2.90	-0.30	+0.52	3.61	-0.01	0.00	3.54	+0.00	-0.01
Fe$_4$	3.12	-0.21	+0.24	3.62	-0.03	+0.01	3.60	-0.01	0.00

On the B surface only the magnetic moments of two Fe atoms, those that are above the iron vacancy in the

third layer, decrease. The reason is the same as for the A surface. As for the A surface, two oxygen atoms

acquire a small magnetic moment ($\sim$0.35 μ_B) but for a process similar to that of the Fe atoms: charge is

transferred from the spin down channel to the spin up one.

Now we pass to investigate the electronic properties of the reduced B′ surface. As shown in Fig. 8c the main effect of the oxygen vacancy is the opening of the electronic gaps: 1.51 eV and 1.66 eV, for the spin up and down gaps, respectively. This is due to the octahedral iron and oxygen states, as shown in Figs. 7d, S6d, and S7d which are now well below the calculated Fermi Energy. The localized surface states in the conduction band disappear, and localized surface states formed instead at the top of the valence band. The B′ surface is semiconducting. The modifications of the band structure from B to B′ are related to the enhanced stability of the reduced B′ structure. Also for the reduced A′ surface the empty localized surface states (not shown) disappear, and the surface is still a semiconductor as the A surface but with larger band gaps.

The magnetic moments of the Fe atoms on the B′ surface are not substantially changed with respect to the bulk, while three oxygen atoms acquired a small magnetic moments ($\sim 0.40 \; \mu_B$).

The analysis of the electronic structure of the investigated surfaces show that the stable maghemite (001) B′ surface is the one whose electronic states and magnetic moment distribution are more similar to the bulk ones.

Conclusions

In this paper we have investigated, using an ab-initio approach based on the density functional theory, the reduction and oxidation properties of maghemite γ-Fe$_2$O$_3$ (001) surfaces. The aim of this work has been to enlighten the role of Fe vacancies on the redox properties of the surfaces. We have considered the Fe vacancies fully beyond the mean-field approach by constructing the surfaces from the maghemite bulk, for which we have taken the lowest energy structure proposed by Crespo et al. [12], whose point group was also found experimentally. We have found that the presence of the Fe vacancies in maghemite increases both the reducibility and the oxidation efficiency of the surfaces. To reach these conclusions we have compared our results for the maghemite surfaces with those for the magnetite ones, that have not iron vacancies in the bulk.

The main effect of the iron vacancies in the proximity of the maghemite surfaces is to decrease the electronic charge of the surface oxygen atoms, both respect to the bulk and to the magnetite surfaces.

The consequence is that the oxygen atoms become easier to remove from the surface, and also easier to adsorb on the surface since the adsorbed atom can lend it some charge. The removal of one surface oxygen from the B surface produces a stable reconstruction which we have termed B$'$. We have calculated the surface stability as a function of temperature and pressure and found that the B$'$ reconstruction is indeed the most stable termination for the maghemite (001) surfaces. We have also considered another reconstruction, termed SVC$_M$, based on the most stable SVC magnetite reconstruction, but we have found that it is slightly less stable than B$'$. Another result that we have obtained is the lower stability of maghemite surfaces with Fe vacancies on the outermost layer. Thus, iron vacancies on the outermost layer tend to destabilize the surfaces. We have also found that the reducibility of the surfaces is strictly related to their stability: more the surface is stable less is reducible. We have examined the charge transfers and the modifications in the electronic structure caused by the reduction of the surfaces.

Our results on the (001) surfaces indicate that maghemite might be a better material than magnetite to use in catalysts for oxidation reactions.

ASSOCIATED CONTENT

Supporting Information

Variation of the oxygen chemical potential $\Delta\mu_O(T,p)$ as function of the temperature (T) and pressure (p) (Fig. S1), side and top view of the R45($\sqrt{2} \times \sqrt{2}$) and of the SVC (001) magnetite surfaces (Fig. S2), variation of the Bader charge of the Fe atoms following the creation of an oxygen vacancy (Table S1), top view of the (2×2) unit cell of A′ surface (Fig. S3), side view of half of the slabs of A, B, B′, and R45($\sqrt{2} \times \sqrt{2}$) surface with an added oxygen atom (Fig. S4), apdos of the Fe atoms of bulk, A surface, B, and B′ surface (Fig. S5), total dos of bulk, A surface, B, and B′ surface (Fig. S6), and band structure of bulk, A surface, B, and B′ surface (Fig. S7).

AUTHOR INFORMATION

Corresponding Author

* E-mail: giulia.righi@unimore.it

ACKNOWLEDGEMENTS

REFERENCES

(1)   Tartaj, P.; Morales, M. P.; Gonzalez-Carreño, T.; Veintemillas-Verdaguer, S.; Serna, C. J. The Iron Oxides Strike Back: From Biomedical Applications to Energy Storage Devices and Photoelectrochemical Water Splitting. *Advanced Materials* **2011**, *23* (44), 5243–5249.

(2)   Munoz, M.; Pedro, Z. M. de; Casas, J. A.; Rodriguez, J. J. Preparation of Magnetite-Based Catalysts and Their Application in Heterogeneous Fenton Oxidation – A Review. *Applied Catalysis B: Environmental* **2015**, *176–177*, 249–265. https://doi.org/10.1016/j.apcatb.2015.04.003.

(3)   Tartaj, P.; Morales, M. P.; González-Carreño, T.; Veintemillas-Verdaguer, S.; Serna, C. J. Advances in Magnetic Nanoparticles for Biotechnology Applications. *Journal of Magnetism and Magnetic Materials* **2005**, *290–291*, 28–34. https://doi.org/10.1016/j.jmmm.2004.11.155.

(4)   Zhou, Q.; Li, J.; Wang, M.; Zhao, D. Iron-Based Magnetic Nanomaterials and Their Environmental Applications. *Critical reviews in environmental science and technology* **2016**, *46* (8), 783–826.

(5)   Mars, P.; Krevelen, D. W. van. Oxidations Carried out by Means of Vanadium Oxide Catalysts. *Chemical Engineering Science* **1954**, *3*, 41–59. https://doi.org/10.1016/S0009-2509(54)80005-4.

(6)   Qiu, K.; Chai, G.; Jiang, C.; Ling, M.; Tang, J.; Guo, Z. Highly Efficient Oxygen Reduction Catalysts by Rational Synthesis of Nanoconfined Maghemite in a Nitrogen-Doped Graphene Framework. *ACS Catalysis* **2016**, *6* (6), 3558–3568.

(7)   Zhou, W.; Ge, L.; Chen, Z.-G.; Liang, F.; Xu, H.-Y.; Motuzas, J.; Julbe, A.; Zhu, Z. Amorphous Iron Oxide Decorated 3D Heterostructured Electrode for Highly Efficient Oxygen Reduction. *Chemistry of Materials* **2011**, *23* (18), 4193–4198. https://doi.org/10.1021/cm201439d.

(8)   Najafishirtari, S.; Guglieri, C.; Marras, S.; Scarpellini, A.; Brescia, R.; Prato, M.; Righi, G.; Franchini, A.; Magri, R.; Manna, L.; Colombo, M. Metal-Support Interaction in Catalysis: The Influence of the Morphology of a Nano-Oxide Domain on Catalytic Activity. *Applied Catalysis B: Environmental* **2018**, *237*, 753–762. https://doi.org/10.1016/j.apcatb.2018.06.033.

(9)   Wang, J.; Zhou, H.; Nanda, J.; Braun, P. V. Three-Dimensionally Mesostructured Fe2O3 Electrodes with Good Rate Performance and Reduced Voltage Hysteresis. *Chemistry of Materials* **2015**, *27* (8), 2803–2811.

(10)   Shokrollahi, H. A Review of the Magnetic Properties, Synthesis Methods and Applications of Maghemite. *Journal of Magnetism and Magnetic Materials* **2017**, *426*, 74–81. https://doi.org/10.1016/j.jmmm.2016.11.033.

(11)   Jubb, A. M.; Allen, H. C. Vibrational Spectroscopic Characterization of Hematite, Maghemite, and Magnetite Thin Films Produced by Vapor Deposition. *ACS Applied Materials & Interfaces* **2010**, *2* (10), 2804–2812.

(12)   Grau-Crespo, R.; Al-Baitai, A. Y.; Saadoune, I.; De Leeuw, N. H. Vacancy Ordering and Electronic Structure of γ-Fe2O3 (Maghemite): A Theoretical Investigation. *Journal of Physics: Condensed Matter* **2010**, *22* (25), 255401.

(13)   Cornell, R. M.; Schwertmann, U. *The Iron Oxides: Structure, Properties, Reactions, Occurrences and Uses*; John Wiley & Sons, 2003.

(14)   Waychunas, G. A. Crystal Chemistry of Oxides and Oxyhydroxides. *Rev.Mineral.Geochem* **1991**, *2511*.

(15)   Van Oosterhout, G.; Rooijmans, C. A New Superstructure in Gamma-Ferric Oxide. *Nature* **1958**, *181* (4601), 44.

(16)   Greaves, C. A Powder Neutron Diffraction Investigation of Vacancy Ordering and Covalence in γ-Fe2O3. *Journal of Solid State Chemistry* **1983**, *49* (3), 325–333.

(17)   Shmakov, A.; Kryukova, G.; Tsybulya, S.; Chuvilin, A.; Solovyeva, L. Vacancy Ordering in γ-Fe2O3: Synchrotron X-Ray Powder Diffraction and High-Resolution Electron Microscopy Studies. *Journal of Applied Crystallography* **1995**, *28* (2), 141–145.

(18)   Jørgensen, J.-E.; Mosegaard, L.; Thomsen, L. E.; Jensen, T. R.; Hanson, J. C. Formation of γ-Fe2O3 Nanoparticles and Vacancy Ordering: An in Situ X-Ray Powder Diffraction Study. *Journal of Solid State Chemistry* **2007**, *180* (1), 180–185.

(19)   Pentcheva, R.; Wendler, F.; Meyerheim, H. L.; Moritz, W.; Jedrecy, N.; Scheffler, M. Jahn-Teller Stabilization of a ?Polar? Metal Oxide Surface: Fe 3 O 4 (001). *Physical review letters* **2005**, *94* (12), 126101.

(20)   Bliem, R.; McDermott, E.; Ferstl, P.; Setvin, M.; Gamba, O.; Pavelec, J.; Schneider, M. A.; Schmid, M.; Diebold, U.; Blaha, P.; et al. Subsurface Cation Vacancy Stabilization of the Magnetite (001) Surface. *Science* **2014**, *346* (6214), 1215–1218. https://doi.org/10.1126/science.1260556.

(21)   Baetzold, R. C.; Yang, H. Computational Study on Surface Structure and Crystal Morphology of γ-Fe2O3: Toward Deterministic Synthesis of Nanocrystals. *The Journal of Physical Chemistry B* **2003**, *107* (51), 14357–14364.

(22)   Guo, P.; Guo, X.; Zheng, C. Roles of γ-Fe2O3 in Fly Ash for Mercury Removal: Results of Density Functional Theory Study. *Applied Surface Science* **2010**, *256* (23), 6991–6996.

(23)   Giannozzi, P.; Baroni, S.; Bonini, N.; Calandra, M.; Car, R.; Cavazzoni, C.; Ceresoli, D.; Chiarotti, G. L.; Cococcioni, M.; Dabo, I.; et al. QUANTUM ESPRESSO: A Modular and Open-Source Software Project for Quantum Simulations of Materials. *Journal of physics: Condensed matter* **2009**, *21* (39), 395502.

(24)   Giannozzi, P.; Andreussi, O.; Brumme, T.; Bunau, O.; Nardelli, M. B.; Calandra, M.; Car, R.; Cavazzoni, C.; Ceresoli, D.; Cococcioni, M.; et al. Advanced Capabilities for Materials Modelling with QUANTUM ESPRESSO. *Journal of Physics: Condensed Matter* **2017**, *29* (46), 465901.

(25)   Perdew, J. P.; Burke, K.; Ernzerhof, M. Generalized Gradient Approximation Made Simple [Phys. Rev. Lett. 77, 3865 (1996)]. *Phys. Rev. Lett.* **1997**, *78* (7), 1396–1396. https://doi.org/10.1103/PhysRevLett.78.1396.

(26)   Cococcioni, M.; de Gironcoli, S. Linear Response Approach to the Calculation of the Effective Interaction Parameters in the $\mathrm{LDA}+\mathrm{U}$ Method. *Phys. Rev. B* **2005**, *71* (3), 035105. https://doi.org/10.1103/PhysRevB.71.035105.

(27)   Xue, P.; Fu, Z.; Chu, X.; Zhang, Y.; Yang, Z. Density Functional Theory Study on the Interaction of CO with the Fe3O4(001) Surface. *Applied Surface Science* **2014**, *317*, 752–759. https://doi.org/10.1016/j.apsusc.2014.09.002.

(28)   Monkhorst, H. J.; Pack, J. D. Special Points for Brillouin-Zone Integrations. *Phys. Rev. B* **1976**, *13* (12), 5188–5192. https://doi.org/10.1103/PhysRevB.13.5188.

(29)   Dronskowski, R. The Little Maghemite Story: A Classic Functional Material. *Advanced Functional Materials* **2001**, *11* (1), 27–29. https://doi.org/10.1002/1616-3028(200102)11:1<27::AID-ADFM27>3.0.CO;2-X.

(30)   Bader, R. F. *Atoms in Molecules*; Wiley Online Library, 1990.

(31)   Löwdin, P. On the Non-Orthogonality Problem Connected with the Use of Atomic Wave Functions in the Theory of Molecules and Crystals. *The Journal of Chemical Physics* **1950**, *18* (3), 365–375. https://doi.org/10.1063/1.1747632.

(32)   Löwdin, P.-O. On the Nonorthogonality Problem**The Work Reported in This Paper Has Been Sponsored in Part by the Swedish Natural Science Research Council, in Part by the Air Force Office of Scientific Research (OSR) through the European Office of Aerospace Research (OAR), U.S. Air Force under Grant AF-EOAR 67-50 with Uppsala University, and in Part by the National Science Foundation under Grant GP-5419 with the University of Florida.; Löwdin, P.-O., Ed.; Advances in Quantum Chemistry; Academic Press, 1970; Vol. 5, pp 185–199. https://doi.org/10.1016/S0065-3276(08)60339-1.

(33)   Reuter, K.; Scheffler, M. Composition, Structure, and Stability of $\mathrm{RuO_2}(110)$ as a Function of Oxygen Pressure. *Phys. Rev. B* **2001**, *65* (3), 035406. https://doi.org/10.1103/PhysRevB.65.035406.

(34)   Reuter, K.; Scheffler, M. Composition and Structure of the RuO 2 (110) Surface in an O 2 and CO Environment: Implications for the Catalytic Formation of CO 2. *Physical Review B* **2003**, *68* (4), 045407.

(35)   Parkinson, G. S. Iron Oxide Surfaces. *Surface Science Reports* **2016**, *71* (1), 272–365.

(36)   Grau-Crespo, R.; Catlow, C. R. A.; Leeuw, N. H. de. A Computer Modeling Study of Redox Processes on the FeSbO4 (100) Surface. *Journal of Catalysis* **2007**, *248* (1), 77–88. https://doi.org/10.1016/j.jcat.2007.02.015.

(37)   Chase, M. W. *NIST-JANAF Thermochemical Tables*; Washington, D.C.: American Chemical

Society ; Woodbury, N.Y. : American Institute of Physics for the National Institute of Standards and Technology, 1998.

(38)   Pentcheva, R.; Moritz, W.; Rundgren, J.; Frank, S.; Schrupp, D.; Scheffler, M. A Combined DFT/LEED-Approach for Complex Oxide Surface Structure Determination: Fe3O4(001). *Surface Science* **2008**, *602* (7), 1299–1305. https://doi.org/10.1016/j.susc.2008.01.006.

(39)   Fonin, M.; Hartung, C.; Rüdiger, U.; Backes, D.; Heyderman, L.; Nolting, F.; Rodríguez, A. F.; Kläui, M. Formation of Magnetic Domains and Domain Walls in Epitaxial Fe3O4(100) Elements (Invited). *Journal of Applied Physics* **2011**, *109* (7), 07D315. https://doi.org/10.1063/1.3540678.

(40)   \Lodziana, Z. Surface Verwey Transition in Magnetite. *Phys. Rev. Lett.* **2007**, *99* (20), 206402. https://doi.org/10.1103/PhysRevLett.99.206402.

(41)   Yu, X.; Zhang, X.; Wang, S.; Feng, G. Adsorption of Au n (N= 1–4) Clusters on Fe 3 O 4 (001) B-Termination. *RSC Advances* **2015**, *5* (56), 45446–45453.

(42)   Mulakaluri, N.; Pentcheva, R.; Scheffler, M. Coverage-Dependent Adsorption Mode of Water on Fe3O4(001): Insights from First Principles Calculations. *The Journal of Physical Chemistry C* **2010**, *114* (25), 11148–11156. https://doi.org/10.1021/jp100344n.

(43)   Rubio-Zuazo, J.; Chainani, A.; Taguchi, M.; Malterre, D.; Serrano, A.; Castro, G. R. Electronic Structure of FeO, γ- Fe 2 O 3, and Fe 3 O 4 Epitaxial Films Using High-Energy Spectroscopies. *Physical Review B* **2018**, *97* (23), 235148.

(44)   Zhao, K.; Tang, H.; Qiao, B.; Li, L.; Wang, J. High Activity of Au/γ-Fe2O3 for CO Oxidation: Effect of Support Crystal Phase in Catalyst Design. *ACS Catalysis* **2015**, *5* (6), 3528–3539.

(45)   Pires, M. dos S.; Nogueira, F. G. E.; Torres, J. A.; Lacerda, L. C. T.; Corrêa, S.; Pereira, M. C.; Ramalho, T. C. Experimental and Theoretical Study on the Reactivity of Maghemite Doped with Cu2+ in Oxidation Reactions: Structural and Thermodynamic Properties towards a Fenton Catalyst. *RSC Adv.* **2016**, *6* (84), 80830–80839. https://doi.org/10.1039/C6RA11032K.

(46)   Gupta, A. K.; Gupta, M. Synthesis and Surface Engineering of Iron Oxide Nanoparticles for Biomedical Applications. *Biomaterials* **2005**, *26* (18), 3995–4021. https://doi.org/10.1016/j.biomaterials.2004.10.012.

(47)   Litter, M. I.; Blesa, M. A. Photodissolution of Iron Oxides. IV. A Comparative Study on the Photodissolution of Hematite, Magnetite, and Maghemite in EDTA Media. *Canadian Journal of Chemistry* **1992**, *70* (9), 2502–2510. https://doi.org/10.1139/v92-316.
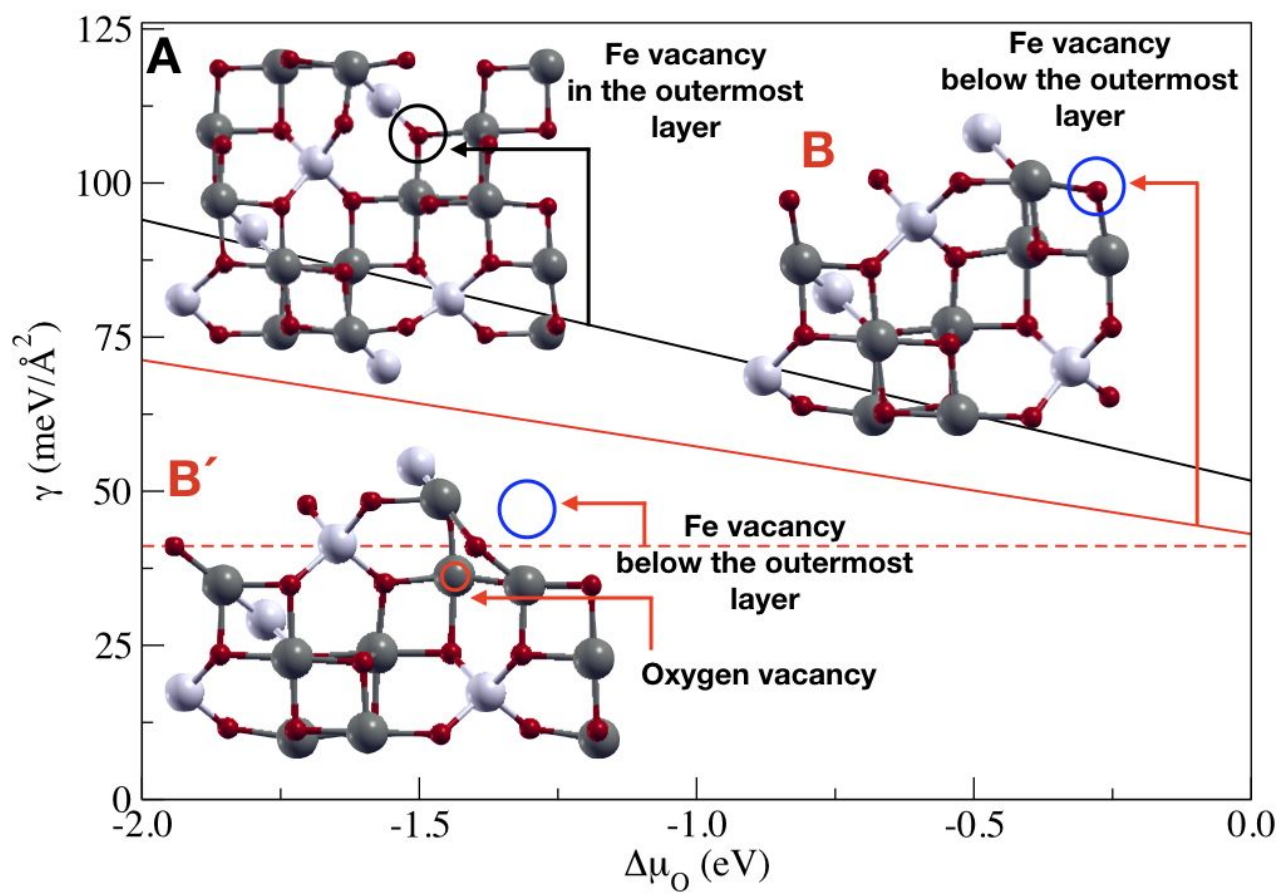
1
2
3
4
5
6
7
8
9
10
11
12
13
14
15
16
17
18
19
20
21
22
23
24
25
26
27
28
29
30
31
32
33
34
35
36
37
38
39
40
41
42
43
44
45
46
47
48
49
50
51
52
53
54
55
56
57
58
59
60

Figure Toc graphic